Primary-Tuning Wireless Constant-Current Charger With Self-Sustained Constant-Voltage Limit Featuring Minimal Secondary Design

Zhicong Huang, *Member, IEEE*, Tian Qin, and Herbert Ho-Ching Iu, *Senior Member, IEEE*

***Abstract*— An inductive power transfer (IPT) converter can operate as a constant-current (CC) source for wireless battery charging. Since the output voltage of a CC power supply linearly increases with the load resistance, a constant-voltage (CV) threshold must be incorporated in the IPT converter, so as to protect the CC power supply from open-load condition and prevent the overvoltage from damaging the battery. This article proposes a primary-tuning IPT converter, which operates as a wireless CC charger with a self-sustained CV limit to feature minimal secondary design. The CC–CV behavior is achieved by only adopting and manipulating a switch-controlled capacitor (SCC) in the primary. Secondary-side control and wireless feedback communication are not necessary, and thus, the secondary is minimal and rugged. A voltage divider circuit helps with reducing the voltage stress of the SCC switches. Soft switching is permitted for all switches throughout the operating range. The operating principle and control scheme of the proposed system are explained. Experimental results are presented to demonstrate the CC–CV behavior of the proposed IPT charger.**

***Index Terms*— Constant current (CC), constant voltage (CV), inductive power transfer (IPT), switch-controlled compensation, wireless charging.**

I. Introduction

INDUCTIVE power transfer (IPT) is a rapidly developing technology to wirelessly deliver power in applications where getting rid of physical contact is desired, e.g., in a hostile environment with heavy dirt and moisture that are dangerous to plugging and unplugging [1], [2], [3]. With the elimination of physical contact, IPT has found viable prospects in wireless battery charging applications [4], [5], [6], [7], [8]. To charge a depleted battery fast, constant-current (CC) charging is commonly used [9]. Since the battery has a voltage threshold based on its chemistry, once the threshold is reached, further CC charging may damage the battery permanently. Therefore, a constant-voltage (CV) limit must be incorporated in the IPT converter that operates as a CC charger. However, the primary and the secondary of the IPT charger are physically separated, and additional efforts should be made to implement the required CC–CV charging profile, which usually complicates the design and control of the secondary. It is still challenging to implement an IPT charger featuring minimal secondary design.

Some approaches have been carried out to achieve the required CC–CV output in IPT converters. It is straightforward to use a multistage scheme where an additional dc/dc converter is cascaded to the IPT converter for output regulation [10], [11], [12], but the power losses incurred by the additional converter stage is a penalty. To simplify the circuit topology as being single stage, the modulation given by the additional dc/dc converter can be alternatively implemented by an active rectifier where active switches are incorporated, but such schemes require more complex control in the secondary [13], [14]. To further ease the control efforts, load-independent-current (LIC) [15] and load-independent-voltage (LIV) [16] transfer characteristics of single-stage IPT converters have been widely investigated for the CC–CV output. The transition from CC to CV can be achieved by either hoping the operating frequencies from the LIC point to the LIV point in an IPT converter designed with a single compensation topology [17], [18] or altering the compensation topologies in an IPT converter that has hybrid compensation circuits [19], [20], [21], [22]. In these and other listed applications, it is necessary to sense the output voltage and regulate it to the limiting value with wireless feedback communication, which increases the control complexity in the secondary and reduces the control reliability, respectively. In addition, overcurrent protection for the series compensated primary is another issue that should be addressed with less dependence on wireless feedback communication [23].

As demonstrated in Fig. 1, the key to the minimal secondary design is the realization of self-sustained transition from CC output to CV output. Huang et al. [24] proposed a passive approach to inherent CC–CV output. The proposed IPT system is based on a three-coil coupler, among which an extra coil together with a rectifier is utilized to clamp the primary-side current. The induced secondary output voltage, therefore, has a limit without the necessity of secondary-side control and

Manuscript received 15 February 2023; revised 3 June 2023; accepted 3 July 2023. Date of publication 7 July 2023; date of current version 3 October 2023. This work was supported in part by the National Natural Science Foundation of China under Grant 52007067 and in part by the Natural Science Foundation of Guangdong Province under Grant 2022A1515011581 and Grant 2023A1515011623. Recommended for publication by Associate Editor Chi Kwan Lee. *(Corresponding author: Zhicong Huang.)*

Zhicong Huang and Tian Qin are with the Shien-Ming Wu School of Intelligent Engineering, South China University of Technology, Guangzhou 510006, China (e-mail: zhiconghuang@scut.edu.cn).

Herbert Ho-Ching Iu is with the School of Electrical, Electronic and Computer Engineering, The University of Western Australia, Crawley, WA 6009, Australia (e-mail: herbert.iu@uwa.edu.au).

Color versions of one or more figures in this article are available at https://doi.org/10.1109/JESTPE.2023.3293021.

Digital Object Identifier 10.1109/JESTPE.2023.3293021

TABLE I
COMPARISONS WITH STATE-OF-THE-ART WORKS

Desirable features	back-end converter [10]–[12]	frequency hopping [17], [18]	hybrid switching [19]–[22]	three-coil coupler [24], [25]	proposed scheme
fixed operating frequency	√	×	√	√	√
none wireless feedback	√	×	×	√	√
none secondary control/sensing	×	×	×	√	√
simple two-coil coupler	√	√	√	×	√
component cost	a dc/dc converter	not necessary	multiple bidirectional switches	a coupler, compensation circuits, a rectifier	two switches
minimal secondary design	×	×	×	√	√

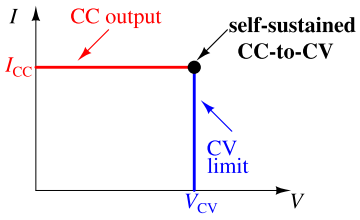

Fig. 1. Self-sustained transition from CC output to CV output for minimal secondary design.

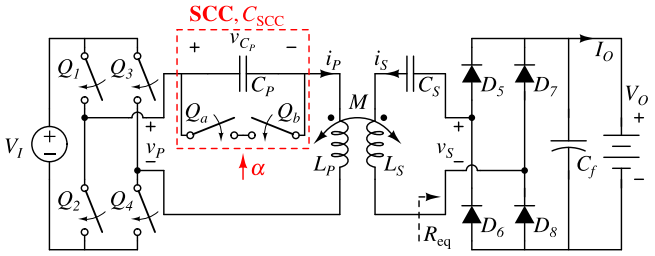

Fig. 2. Proposed wireless battery charger. (Q_a, Q_b, and Q_1–Q_4 represent MOSFET switches with antiparallel diode.)

wireless feedback communication. However, cross coupling between the extra coil and the secondary coil, which cannot be fully eliminated even with careful coupler design, leads to a significant deviation in the CV limit [25].

To overcome the difficulty in the design of three-coil coupler [24], [25], this article proposes a novel active approach to the achievement of native CC output and CV limit in an IPT converter. Comparisons with state-of-the-art works are concluded in Table I. To eliminate the complex design of three-coil coupler, the IPT converter adopts a conventional two-coil coupler with series–series (SS) compensation, and it operates as a CC charger. The primary adopts a switch-controlled capacitor (SCC) for active tuning of the primary tank impedance, such that CV limits in the secondary can be readily achieved once the primary tank current reaches its maximum. Such an approach enables minimal and rugged secondary design, because the secondary control and wireless feedback communication are not necessary. Moreover, the proposed scheme can cope with open-circuit protection issue for the primary under the removal of the secondary.

The rest of this article is organized as follows. Section II presents the proposed IPT charger and details its operating principle. Section III optimizes the voltage stress of the SCC switches while ensuring the capability of self-sustained CC–CV charging profile and illustrates the control scheme. In Section IV, in addition to steady-state measurement of the proposed system, transient responses against step-load change, misalignment, and removal of the secondary are also validated. Finally, Section V makes a conclusion.

II. PROPOSED SYSTEM AND OPERATING PRINCIPLE

A. Primary SCC Compensated IPT Converter

Fig. 2 depicts the schematics of the proposed wireless charger. The magnetic coupler has primary self-inductance L_P, secondary self-inductance L_S, and mutual inductance M. Series compensation is adopted on both sides of the magnetic coupler, but different from a conventional SS IPT converter [17], an SCC, as highlighted in the red dashed box, is adopted and manipulated in the primary for active tuning of the primary resonant tank. DC voltage source V_I is chopped into ac voltage v_P to drive the primary tank circuit at a fixed operating frequency ω by a full-bridge inverter. The secondary ac output is rectified to charge the battery. V_O and I_O are the output voltage and current, respectively. For steady-state analysis, the load can be modeled as a resistor determined by $R_L = (V_O/I_O)$.

For simplicity, the secondary operates as a resonant tank at ω, by fully compensating L_S with C_S that can be designed as follows:

$$C_S = \frac{1}{\omega^2 L_S}. \tag{1}$$

The SCC includes a capacitor C_P in parallel with two antiseries connected MOSFET switches Q_a and Q_b. Without modulating Q_a and Q_b, C_P should resonate with L_P at ω, as given by

$$C_P = \frac{1}{\omega^2 L_P} \tag{2}$$

whereas the control of Q_a and Q_b can steplessly vary the equivalent capacitance C_{SCC}.

Modulation of the SCC has been detailed in [26], [27], and [28], and the typical switching sequence and operating waveforms are given in Fig. 3. Gate driving signals of Q_a and Q_b have phase shift $\alpha \in [(\pi/2), \pi]$ from i_P and are complementary to each other. Q_a and Q_b are turned on and off at zero voltage for low switching loss. v_{C_P} is shaped as part of a sine wave, and effective charging/discharging time of C_P in half a cycle is $2(\pi - \alpha)$. As the dashed curve labeled with $v_{C_P,1}$, the increase of α will decrease the peak of the

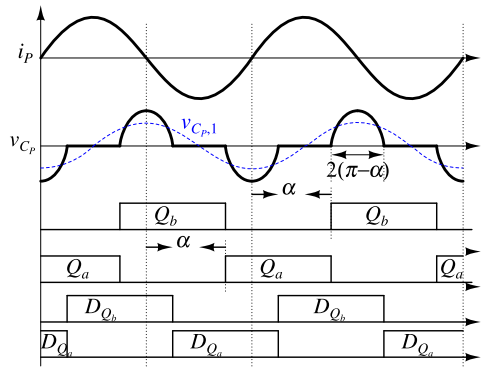

Fig. 3. Switch sequences and operating waveforms of the SCC (D_{Q_a} and D_{Q_b} are the antiparallel diodes of Q_a and Q_b, respectively).

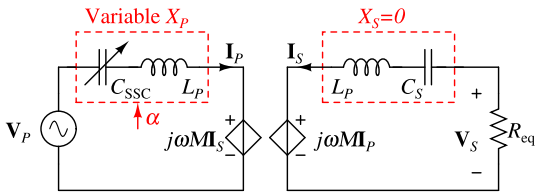

Fig. 4. Fundamental circuit model of the proposed system.

fundamental component of v_{C_P}. Consequently, the equivalent capacitance C_{SCC} of the SCC can be varied by the phase-shift angle α. Equivalent C_{SCC} can be derived by considering the fundamental components of v_{C_P} and i_P, as given by

$$C_{\text{SCC}} = \frac{C_P}{2-(2\alpha-\sin 2\alpha)/\pi}. \tag{3}$$

Using fundamental approximation, an equivalent circuit model of the proposed system is shown in Fig. 4. It is similar to that of the conventional SS IPT converter, except for the switch-controlled primary tank circuit. The secondary tank circuit has null reactance

$$X_S = X_{L_S} + X_{C_S} = 0 \tag{4}$$

where $X_{L_S} = \omega L_S$ and $X_{C_S} = -1/(\omega C_S)$. In the rest of this article, $X_{\text{subscript}}$ represents corresponding reactance indicated by its subscript.

Variable reactance of the primary tank circuit controlled by α is given by

$$X_P = X_{L_P} + X_{C_{\text{SCC}}} \tag{5}$$

$$= \frac{2\alpha-\sin 2\alpha-\pi}{\pi} X_{L_P} \tag{6}$$

where $X_{L_P} = \omega L_P$ and $X_{C_{\text{SCC}}} = -1/(\omega C_{\text{SCC}})$. Based on (3) and (6), when α is varied from 0.5π to π, the capacitive reactance $X_{C_{\text{SCC}}}$ can be modulated from X_{C_P} toward zero, resulting in the monotonic increase of X_P from zero to X_{L_P}, as shown in Fig. 5.

In Fig. 4, $\mathbf{V}_P$, $\mathbf{I}_P$, $\mathbf{V}_S$, and $\mathbf{I}_S$ are vectors of fundamentals of v_P, i_P, v_S, and i_S, respectively. $R_{\text{eq}} = (8/\pi^2)R_L$ is defined as the equivalent load resistance of the rectifier as well as the load. The system equations are given by

$$\mathbf{V}_P = jX_M\mathbf{I}_S + jX_P\mathbf{I}_P \tag{7}$$

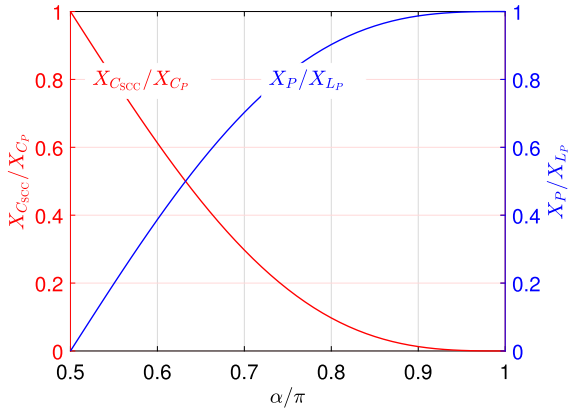

Fig. 5. Normalized $X_{C_{\text{SCC}}}$ and X_P versus α.

and

$$\mathbf{V}_S = -R_{\text{eq}}\mathbf{I}_S = jX_M\mathbf{I}_P \tag{8}$$

where $X_M = \omega M$.

B. Native CC Output ($\alpha = \pi/2$)

When the primary tank current $|\mathbf{I}_P|$ is within its maximum value, modulation of the SCC is not needed, i.e.,

$$\alpha = \pi/2, \quad \text{for } |\mathbf{I}_P| \le |\mathbf{I}_P|_{\max} \tag{9}$$

where $|\mathbf{I}_P|_{\max}$ is subject to desired CV threshold $|\mathbf{V}_S|_{\text{th}}$, and with (8), it is given by

$$|\mathbf{I}_P|_{\max} = \frac{|\mathbf{V}_S|_{\text{th}}}{X_M}. \tag{10}$$

By substituting (9) into (6), the primary tank circuit has null reactance as follows:

$$X_P = 0, \quad \text{for } \alpha = \pi/2. \tag{11}$$

With (4) and (11), both the primary and the secondary are fully compensated at the operating frequency ω, such that the proposed system operates as the conventional SS IPT converter. By substituting (11) into (7) and (8), the native CC output can be derived as follows:

$$|\mathbf{I}_S| = \frac{|\mathbf{V}_P|}{X_M}, \quad \text{for } \alpha = \pi/2. \tag{12}$$

The primary tank current given by (13) will linearly increase with the load resistance R_{eq} during the CC charging process

$$|\mathbf{I}_P| = \frac{|\mathbf{V}_P|}{X_M^2} R_{\text{eq}} \le |\mathbf{I}_P|_{\max}. \tag{13}$$

C. Operating Principle of Self-Sustained CV Limits (Variable $\alpha > \pi/2$)

To restrict the primary tank current $|\mathbf{I}_P|$ to its maximum value $|\mathbf{I}_P|_{\max}$ for the desired CV threshold, modulation of the SCC is needed. With (7), variable α can be derived by solving

$$\frac{|\mathbf{V}_P|}{\sqrt{\left(\frac{X_M^2}{R_{\text{eq}}}\right)^2 + X_P^2}} = |\mathbf{I}_P|_{\max}. \tag{14}$$

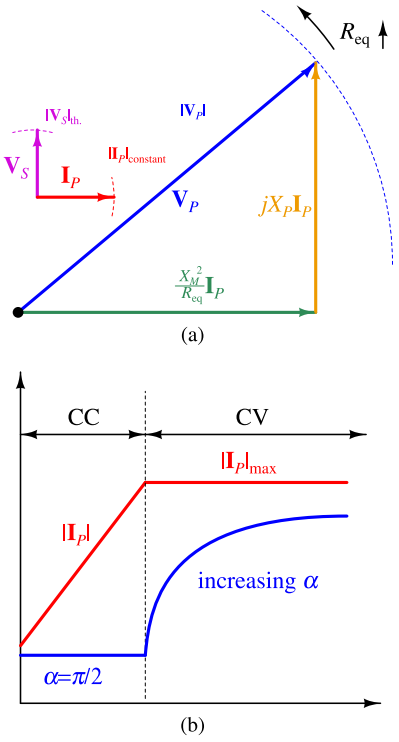

Fig. 6. (a) Phasor diagram of the primary tank circuit. (b) Variation of α and $|\mathbf{I}_P|$ throughout the whole charging process.

It can also be illustrated by a phasor diagram shown in Fig. 6(a). Dashed curves represent the amplitude limits of corresponding phasors. The counterclockwise rotation represents the increase of R_{eq}. To satisfy (14), X_P should be correspondingly increased to offset the decrease of (X_M^2/R_{eq}) caused by the increase of R_{eq} during the CV charging process. From Fig. 5, it can be done via the control of α.

Therefore, the overall operating principle for the desired CC–CV behavior is indicated in Fig. 6(b). For the initial CC charging, α is kept at $\pi/2$ when $|\mathbf{I}_P| < |\mathbf{I}_P|_{\max}$. Later, α begins to increase from $\pi/2$ to maintain $|\mathbf{I}_P| = |\mathbf{I}_P|_{\max}$ for the CV threshold given by

$$|\mathbf{V}_S|_{\text{th}} = |\mathbf{I}_P|_{\max} X_M. \tag{15}$$

III. Design Consideration and Control Scheme

A. Voltage Stress Reduction of SCC Switches

According to Figs. 5 and 6(b), the maximum voltage across the SCC occurs at the transition from the CC output to the CV output, where there is no modulation in the SCC, i.e., $X_{C_{\text{SCC}}} = X_{C_P}$. Thus, the voltage stress of the SCC switches shown in Fig. 2 can be calculated as follows:

$$|\mathbf{V}_{\text{SCC}}|_{\max} = |\mathbf{I}_P|_{\max} X_{C_P}. \tag{16}$$

It can be observed that the voltage stress $|\mathbf{V}_{\text{SCC}}|_{\max}$ can be optimized via the reduction of X_{C_P}.

In order to reduce the voltage stress of the SCC switches, a voltage divider can be designed for the SCC, as shown in Fig. 7. To be specific, the sole SCC in Fig. 2 can be reconfigured as a new SCC with voltage divider. C'_P is the new capacitor in the SCC circuit. As usual, C'_P is in parallel

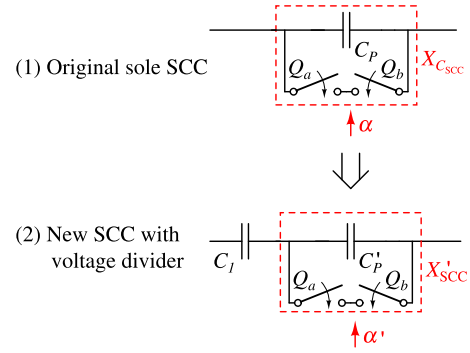

Fig. 7. Voltage divider circuit of new SCC.

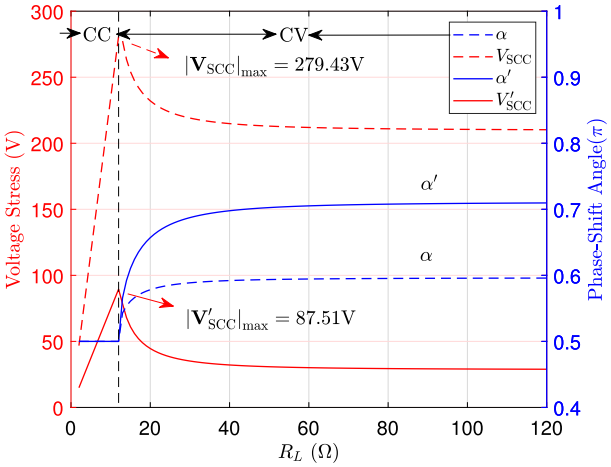

Fig. 8. Simulated voltage stress ($|\mathbf{V}_{\text{SCC}}|_{\max}$ and $|\mathbf{V}'_{\text{SCC}}|_{\max}$) and phase-shift angle (α and α') versus equivalent load resistance R_L.

with two antiseries connected MOSFET switches, and the equivalent impedance of the new SCC is donated as X'_{SCC}, which is tunable via the phase-shift angle α'. C_1 is the fixed-value capacitor, and its impedance is given by X_{C_1}. Similarly, at the transition from the CC output to the CV output, there is no modulation in the SCC, i.e., $X'_{\text{SCC}} = X'_{C_P}$. The voltage stress of the new SCC switches shown in Fig. 7 can be calculated as follows:

$$\left|\mathbf{V}'_{\text{SCC}}\right|_{\max} = |\mathbf{I}_P|_{\max} X'_{C_P}. \tag{17}$$

In addition, the new SCC together with C_1 donates an identical impedance to keep the primary resonant as given by

$$X_{C_1} + X'_{C_P} = X_{C_P} = -X_{L_P}. \tag{18}$$

With (17) and (18), the increase of X_{C_1} can help with the reduction of voltage stress of the SCC switches.

Based on the operating principle of SCC, the impedance of the new SCC varies within

$$X'_{\text{SCC}} \in \left[X'_{C_P}, 0\right). \tag{19}$$

The new variable reactance of the primary tank and its range are given by

$$X'_P = X_{L_P} + X_{C_1} + X'_{\text{SCC}} \in [0, X_{L_P} + X_{C_1}). \tag{20}$$

To satisfy the operating principle, as shown in Fig. 6(a), X'_P should be tunable and capable to vary in a sufficiently wide

TABLE II
CIRCUIT PARAMETERS FOR SIMULATION

Parameters	Symbols	Values
Self inductance	L_P,L_S	66 μH, 58 μH
Mutual inductance	M	20 μH
Equivalent load resistance	R_{eq}	2 Ω to 120 Ω
Operating frequency	$\omega/2\pi$	85 kHz
(1) Sole SCC	C_P	53 nF
(2) SCC with voltage divider	C_1 C'_P	83 nF 150 nF

range, such that $|\mathbf{I}_P|_{\max}$ can be maintained throughout a wide range of R_{eq}. Given $R_{\text{eq}} \in [R_{\text{eq,min}}, R_{\text{eq,max}}]$, a maximum value of X'_P is desired at $R_{\text{eq,max}}$ according to (14) and Fig. 6(b). Thus, X'_P should satisfy

$$X'_P \geq \sqrt{\left(\frac{|\mathbf{V}_P|}{|\mathbf{I}_P|_{\max}}\right)^2 - \left(\frac{X_M^2}{R_{\text{eq,max}}}\right)^2}. \tag{21}$$

With (20) and (21), X_{C_1} can be designed within a range given by

$$X_{C_1} \geq \sqrt{\left(\frac{|\mathbf{V}_P|}{|\mathbf{I}_P|_{\max}}\right)^2 - \left(\frac{X_M^2}{R_{\text{eq,max}}}\right)^2} - X_{L_P}. \tag{22}$$

Thus, once the maximum value of X_{C_1} is designed, the minimum voltage stress of the SCC switches can be achieved as follows:

$$\min\left(\left|\mathbf{V}'_{\text{SCC}}\right|_{\max}\right) = |\mathbf{I}_P|_{\max}\sqrt{\left(\frac{|\mathbf{V}_P|}{|\mathbf{I}_P|_{\max}}\right)^2 - \left(\frac{X_M^2}{R_{\text{eq,max}}}\right)^2}. \tag{23}$$

To demonstrate the voltage stress reduction of SCC switches, a simulation is conducted to compare $|\mathbf{V}_{\text{SCC}}|_{\max}$ and $|\mathbf{V}_{\text{SCC}}|'_{\max}$, as shown in Fig. 8. The simulation parameters of the original SCC and the new SCC with voltage divider are given in Table II. α and α' are the phase-shift angles of the original SCC and the new SCC with voltage divider, respectively, and they are modulated against the variation of load conditions to restrict the $\mathbf{I}_P$ within an identical threshold value $|\mathbf{I}_P|_{\max}$ for an identical CV output. The red solid and dashed curves show the voltage stress of the original SCC and the new SCC with voltage divider during the whole charging process, respectively. It can be observed that the voltage stress can be significantly reduced with the help of X_{C_1}.

B. Control Scheme

Based on the operation of α given in Sections II-B and II-C, Fig. 9 shows the control diagram in practical implementation. Since the operating frequency in the primary is fixed, the ideal SS IPT converter has its own CC output characteristics, in order to achieve a CV output when the load varies, and only the control of the SCC in the primary is needed for the proposed charger. Wireless feedback communication between the primary and the secondary can be eliminated. The zero-crossing point and the amplitude of primary tank circuit current i_P are detected. Zero-crossing detection of i_P generates a synchronization signal for the SCC PWM generations. $|\mathbf{I}_P|$ takes a monotonic relationship with the control variable α'. Therefore, a simple PI controller applies the correction to the difference between $|\mathbf{I}_P|$ and $|\mathbf{I}_P|_{\max}$ and forms a control signal α' for the SCC. It should be noted that, an amplitude limiter is used for α', such that the control scheme is also applicable during the CC charging process.

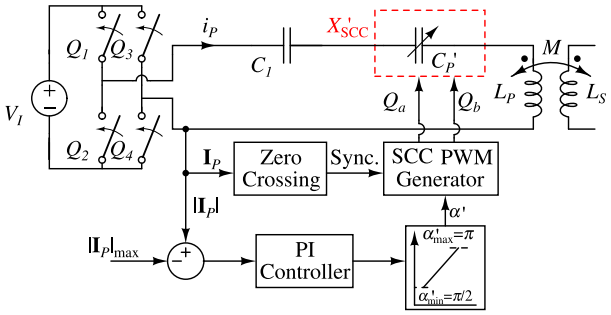

Fig. 9. Control diagram of the proposed system.

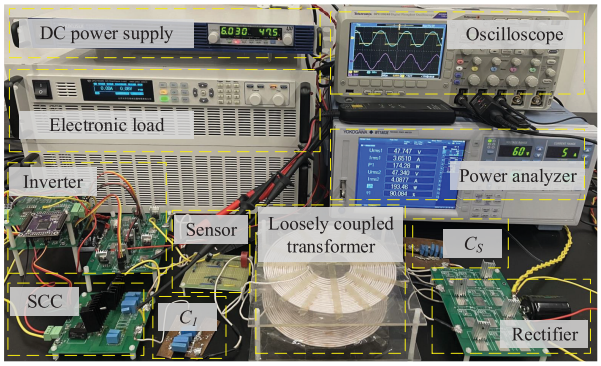

Fig. 10. Experimental setup.

TABLE III
PARAMETERS OF THE EXPERIMENTAL PROTOTYPE

Parameters	Symbols	Measured Values
Input voltage	V_I	48 V
Inverter switches	Q_1-Q_4	IRF640
SCC switches	Q_a,Q_b	IPW60R045
Diodes	D_1-D_4	MBR20200
Self inductance	L_P,L_S	65.8 μH, 59.1 μH
Mutual inductance	M	19.2 μH
Equivalent load resistance	R_{eq}	2 Ω to 120 Ω
Operating frequency	$\omega/2\pi$	85 kHz
(1) Sole SCC	C_P	53.4 nF
(2) SCC with voltage divider	C_1 C'_P	80.2 nF 156.3 nF

IV. EXPERIMENTAL VERIFICATION

To verify the CC–CV behavior of the proposed system, two experimental prototypes are built with a sole SCC and an SCC with a voltage divider. The parameters are given in Table III, and the experimental setup is shown in Fig. 10. Given a battery with a capacity of 10 Ah and a nominal voltage of 48 V, the desired charge current and the charge threshold voltage can be fixed to $I_O = 4$ A and $V_O = 52$ V separately. An electronic load is used to emulate the battery. The closed-loop primary current control scheme demonstrated in Section III-B is implemented in a microcontroller for CC–CV charging throughout the charging process.

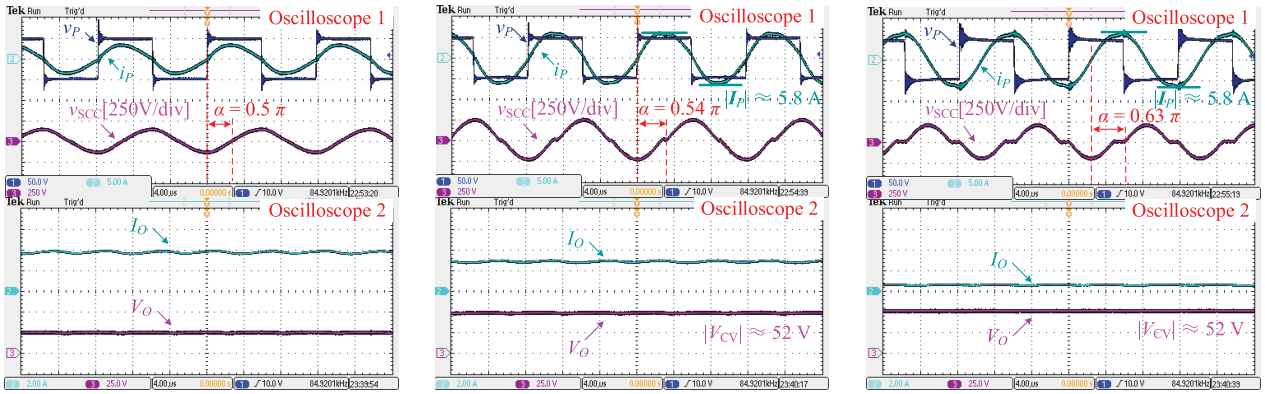

(a) (b) (c)

Fig. 11. Measured steady-state operating waveforms with a sole SCC. (a) CC ($R_L = 6\ \Omega$). (b) CV in heavy-load condition ($R_L = 15\ \Omega$). (c) CV in light-load condition ($R_L = 80\ \Omega$).

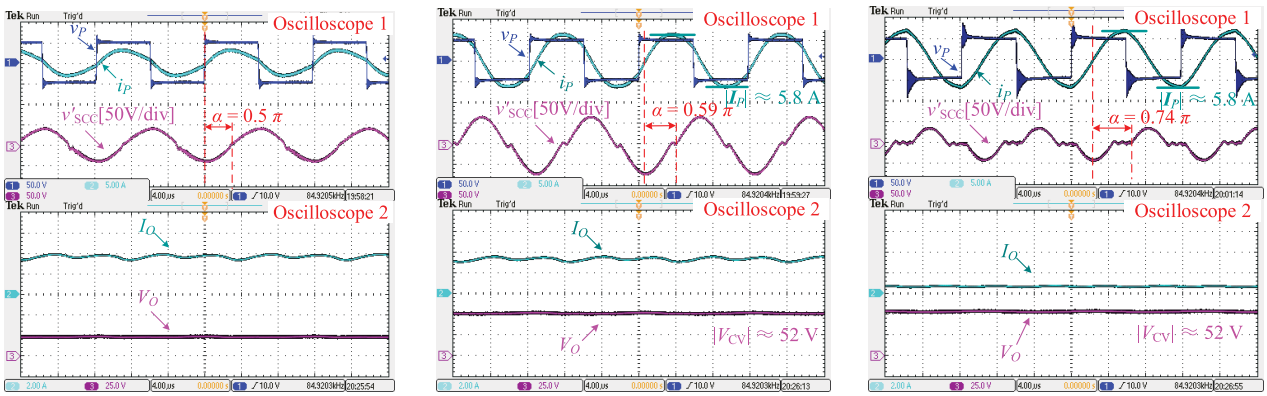

(a) (b) (c)

Fig. 12. Measured steady-state operating waveforms with an SCC with a voltage divider for voltage stress reduction. (a) CC ($R_L = 6\ \Omega$. (b) CV in heavy-load condition ($R_L = 15\ \Omega$). (c) CV in light-load condition ($R_L = 80\ \Omega$).

A. Steady-State Operating Waveforms and Voltage Stress Reduction

Fig. 11 shows the captured steady-state operating waveforms under different charging modes with a sole SCC. The SCC does not operate in the CC mode, as shown in Fig. 11(a), and thus, the system operates as a conventional SS IPT converter to achieve a CC output. The steady-state waveforms in the CV mode (heavy- and light-load conditions) are shown in Fig. 11(b) and (c), where the primary side current $|\mathbf{I}_P|$ is limited to 5.8 A via the tuning of the SCC, such that a CV output being about 52 V is achieved. It can be observed that during CC charging, the phase shift $\alpha = 0.5\pi$, during CV mode, the phase shift α increases with increasing R_L. The maximum voltage stress of the SCC switches occurs at the transition from the CC charging to the CV charging, which can be estimated as being about 258.24 V from Fig. 11(b).

Similarly, Fig. 11 shows the captured steady-state operating waveforms under different charging stages with an SCC with a voltage divider. It can be observed that the operation of the phase-shift angle α' against the load variation is similar to that of α in Fig. 11. The maximum voltage stress of the SCC switches occurs at the transition from the CC charging to the CV charging, which can be estimated as being about 69.25 V from Fig. 12(b). Compared with that in Fig. 11(b), the voltage stress is reduced by up to 73.18%.

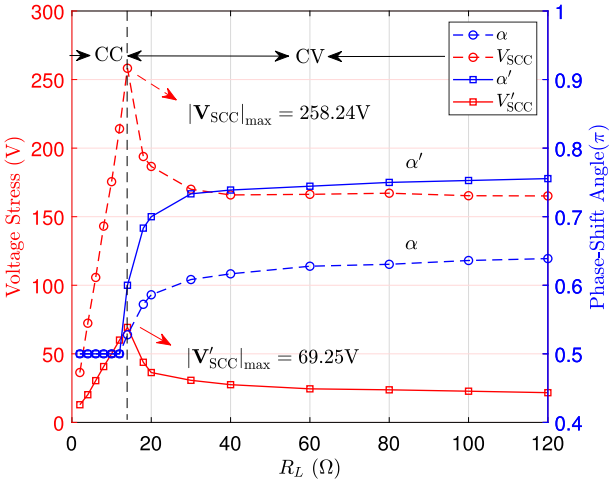

Fig. 13. Measured voltage stress ($|\mathbf{V}_{SCC}|_{max}$ and $|\mathbf{V}'_{SCC}|_{max}$) and phase-shift angle (α and α') versus equivalent load resistance R_L.

Curves of voltage stress against the load variation with the sole SCC and the SCC with voltage divider are also plotted in Fig. 13. Measured α and α' are marked with "◯" and "□"

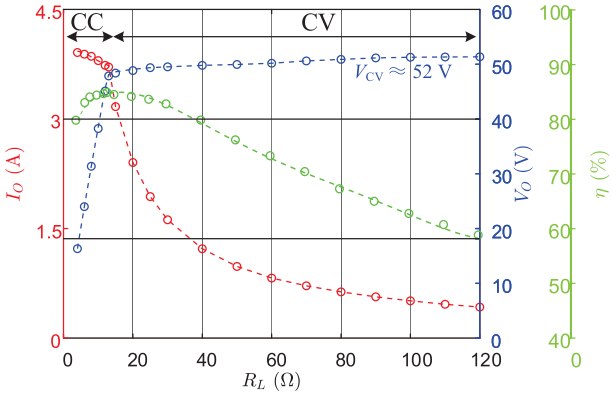

Fig. 14. Measured output current I_O, output voltage V_O, and efficiency η versus equivalent load resistance R_L, with a nominal CC output of $I_{CC} \approx 4$ A and nominal CV limits of $V_{CV} \approx 52$ V.

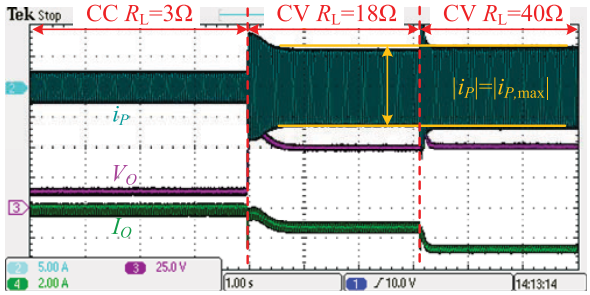

Fig. 15. Transient waveforms for R_L step changing from 3 to 18 Ω and to from 18 to 40 Ω.

in blue, respectively, while measured $\mathbf{V}_{SCC}$ and $\mathbf{V}'_{SCC}$ are marked with "◯" and "□" in red, respectively. In the CC charging stage, both α and α' are held constant at 0.5π, and the voltages $\mathbf{V}_{SCC}$ and $\mathbf{V}'_{SCC}$ increase linearly with the equivalent load resistance. Once the CC charging is transited to the CV charging, the phase-shift angles α and α' increase for a CV output. $\mathbf{V}_{SCC}$ and $\mathbf{V}'_{SCC}$ first increase during the CC charging stage and then decrease during the CV charging stage, and they reach the maximum at the transition from CC charging to the CV charging. It is readily to observe that the voltage stress can be significantly reduced with an SCC with a voltage divider.

With the SCC with a voltage divider, measured output current I_O, output voltage V_O, and efficiency η under equivalent load resistance R_L are in new SCC state, as shown in Fig. 14. The measured output current ranges from 3.94 to 3.78 A. The CV limit is configured via the control reference of $|\mathbf{I}_P|_{max}$, and the measured voltage outputs range from 48.7 to 51.5 V.

B. Transient Responses Against Load Change

Transient waveforms for step-load change are shown in Fig. 15. The primary current i_P, output voltage V_O, and output current I_O are shown as CH_2 in dark green, CH_3 in magenta, and CH_4 in light green, respectively. The load resistance is step changed from 3 to 18 Ω and from 18 to 40 Ω. When $R_L = 3$ Ω, the magnitude of i_P is smaller than its maximum value 5.8 A, and thus, the IPT converter operates as a CC charger. When R_L is step changed to 18 and 40 Ω, the magnitude of i_P is tightly limited to its maximum value 5.8 A,

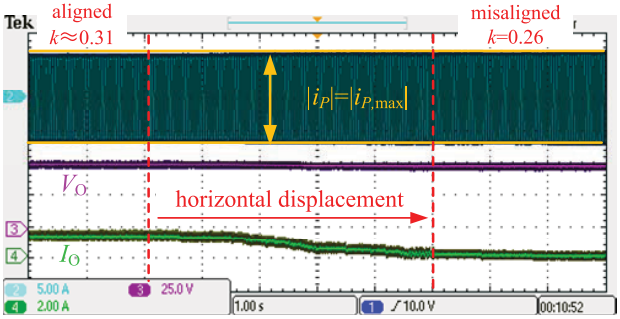

Fig. 16. Transient waveforms against the slow horizontal displacement of the secondary coupler from the aligned position ($k \approx 0.31$) to the misaligned position ($k \approx 0.26$).

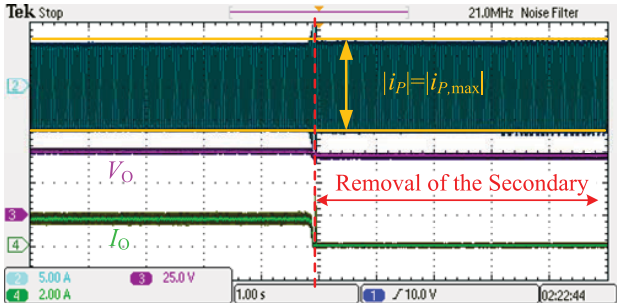

Fig. 17. Transient waveforms for removal of the secondary.

and in the same way, V_O is tightly limited to a threshold value 52 V, as shown in Fig. 15.

C. Transient Responses Against Misalignment

Transient waveforms for misalignment are shown in Fig. 16. The electronic load operates in CV mode (48 V) in series with a 1-Ω resistor to emulate the battery. The secondary coupler is slowly displaced from an aligned position ($k \approx 0.31$) to a misaligned position ($k \approx 0.26$). The primary current i_P, output voltage V_O, and output current I_O are shown as CH_2 in dark green, CH_3 in magenta, and CH_4 in light green, respectively. The magnitude of i_P is tightly limited to its maximum value 5.8 A. The output current I_O shown by CH_4 in light green decreases during the displacement. It validates that, with the tightly fixed i_P, the induced output voltage V_O decreases with the decrease of k due to misalignment, and thus, there is no overvoltage risk for the battery. V_O is later clamped by the battery voltage V_{Bat} once $V_O \leq V_{Bat}$, and I_O becomes zero.

D. Transient Responses Under Removal of the Secondary

Transient waveforms for removal of the secondary are shown in Fig. 17. The electronic load operates in CV mode (48 V) in series with a 1-Ω resistor to emulate the battery. The secondary coupler is instantaneously removed from the aligned position. The primary current i_P, output voltage V_O, and output current I_O are shown as CH_2 in dark green, CH_3 in magenta, and CH_4 in light green, respectively. The output current I_O soon reaches zero, while the output voltage V_O is clamped by the battery voltage V_{Bat}. Nevertheless, the magnitude of i_P is tightly limited to its

maximum value 5.8 A, and thus, there is no overcurrent risk for the primary inverter despite the removal of the secondary.

V. Conclusion

An active IPT approach to native CC output and CV limit is proposed for battery charging applications. Compared with the existing scheme, complex three-coil coupler is not needed. The CC–CV behavior is achieved by only adopting and manipulating switch-controlled compensation in the primary. It eliminates the necessity of secondary control and wireless communication to make the secondary minimal and rugged. The primary faces no open-circuit risk, and all switches can realize soft switching. A voltage divider helps with the voltage stress reduction of the SCC switches. Operating principle and control scheme of the proposed system are illustrated in detail. Experimental results validate the theoretical analysis well.

References

[1] G. A. Covic and J. T. Boys, "Inductive power transfer," *Proc. IEEE*, vol. 101, no. 6, pp. 1276–1289, Jun. 2013.

[2] J. T. Boys and G. A. Covic, "The inductive power transfer story at the University of Auckland," *IEEE Circuits Syst. Mag.*, vol. 15, no. 2, pp. 6–27, 2nd Quart., 2015.

[3] C. C. Mi, G. Buja, S. Y. Choi, and C. T. Rim, "Modern advances in wireless power transfer systems for roadway powered electric vehicles," *IEEE Trans. Ind. Electron.*, vol. 63, no. 10, pp. 6533–6545, Oct. 2016.

[4] S. Y. R. Hui and W. W. C. Ho, "A new generation of universal contactless battery charging platform for portable consumer electronic equipment," *IEEE Trans. Power Electron.*, vol. 20, no. 3, pp. 620–627, May 2005.

[5] S. Lukic and Z. Pantic, "Cutting the cord: Static and dynamic inductive wireless charging of electric vehicles," *IEEE Electrific. Mag.*, vol. 1, no. 1, pp. 57–64, Sep. 2013.

[6] R. Bosshard and J. W. Kolar, "Inductive power transfer for electric vehicle charging: Technical challenges and tradeoffs," *IEEE Power Electron. Mag.*, vol. 3, no. 3, pp. 22–30, Sep. 2016.

[7] S. Y. Hui, "Planar wireless charging technology for portable electronic products and Qi," *Proc. IEEE*, vol. 101, no. 6, pp. 1290–1301, Jun. 2013.

[8] W. X. Zhong, X. Liu, and S. Y. R. Hui, "A novel single-layer winding array and receiver coil structure for contactless battery charging systems with free-positioning and localized charging features," *IEEE Trans. Ind. Electron.*, vol. 58, no. 9, pp. 4136–4144, Sep. 2011.

[9] A. A.-H. Hussein and I. Batarseh, "A review of charging algorithms for nickel and lithium battery chargers," *IEEE Trans. Veh. Technol.*, vol. 60, no. 3, pp. 830–838, Mar. 2011.

[10] A. Berger, M. Agostinelli, S. Vesti, J. A. Oliver, J. A. Cobos, and M. Huemer, "A wireless charging system applying phase-shift and amplitude control to maximize efficiency and extractable power," *IEEE Trans. Power Electron.*, vol. 30, no. 11, pp. 6338–6348, Nov. 2015.

[11] Z. Li, C. Zhu, J. Jiang, K. Song, and G. Wei, "A 3-kW wireless power transfer system for sightseeing car supercapacitor charge," *IEEE Trans. Power Electron.*, vol. 32, no. 5, pp. 3301–3316, May 2017.

[12] J. Liu, Z. Liu, W. Chen, X. Sun, and H. Su, "An optimized coil array and passivity-based control for receiving side multilevel connected DC–DC converter of dynamic wireless charging," *IEEE Trans. Veh. Technol.*, vol. 71, no. 4, pp. 3715–3726, Apr. 2022.

[13] Q. Chen, L. Jiang, J. Hou, X. Ren, and X. Ruan, "Research on bidirectional contactless resonant converter for energy charging between EVs," in *Proc. 39th Annu. Conf. IEEE Ind. Electron. Soc. (IECON)*, Vienna, Austria, Nov. 2013, pp. 1236–1241.

[14] Z. Huang, D. Wang, and X. Qu, "A novel IPT converter with current-controlled semi-active rectifier for efficiency enhancement throughout supercapacitor charging process," *IEEE J. Emerg. Sel. Topics Power Electron.*, vol. 10, no. 2, pp. 2201–2209, Apr. 2022.

[15] W. Zhang, S. Wong, C. K. Tse, and Q. Chen, "Load-independent duality of current and voltage outputs of a series- or parallel-compensated inductive power transfer converter with optimized efficiency," *IEEE J. Emerg. Sel. Topics Power Electron.*, vol. 3, no. 1, pp. 137–146, Mar. 2015.

[16] W. Zhang, S. Wong, C. K. Tse, and Q. Chen, "Analysis and comparison of secondary series- and parallel-compensated inductive power transfer systems operating for optimal efficiency and load-independent voltage-transfer ratio," *IEEE Trans. Power Electron.*, vol. 29, no. 6, pp. 2979–2990, Jun. 2014.

[17] Z. Huang, S. Wong, and C. K. Tse, "Design of a single-stage inductive-power-transfer converter for efficient EV battery charging," *IEEE Trans. Veh. Technol.*, vol. 66, no. 7, pp. 5808–5821, Jul. 2017.

[18] V. Vu, D. Tran, and W. Choi, "Implementation of the constant current and constant voltage charge of inductive power transfer systems with the double-sided LCC compensation topology for electric vehicle battery charge applications," *IEEE Trans. Power Electron.*, vol. 33, no. 9, pp. 7398–7410, Sep. 2018.

[19] X. Qu, H. Han, S. Wong, C. K. Tse, and W. Chen, "Hybrid IPT topologies with constant current or constant voltage output for battery charging applications," *IEEE Trans. Power Electron.*, vol. 30, no. 11, pp. 6329–6337, Nov. 2015.

[20] R. Mai, Y. Chen, Y. Li, Y. Zhang, G. Cao, and Z. He, "Inductive power transfer for massive electric bicycles charging based on hybrid topology switching with a single inverter," *IEEE Trans. Power Electron.*, vol. 32, no. 8, pp. 5897–5906, Aug. 2017.

[21] K. Song, Z. Li, J. Jiang, and C. Zhu, "Constant current/voltage charging operation for series–series and series–parallel compensated wireless power transfer systems employing primary-side controller," *IEEE Trans. Power Electron.*, vol. 33, no. 9, pp. 8065–8080, Sep. 2018.

[22] C. Auvigne, P. Germano, D. Ladas, and Y. Perriard, "A dual-topology ICPT applied to an electric vehicle battery charger, in *Proc. Int. Conf. Electr. Mach.,* 2012, pp. 2287–2292.

[23] W. Li, H. Zhao, J. Deng, S. Li, and C. C. Mi, "Comparison study on SS and double-sided LCC compensation topologies for EV/PHEV wireless chargers," *IEEE Trans. Veh. Technol.*, vol. 65, no. 6, pp. 4429–4439, Jun. 2016.

[24] Z. Huang, G. Wang, J. Yu, and X. Qu, "A novel clamp coil assisted IPT battery charger with inherent CC-to-CV transition capability," *IEEE Trans. Power Electron.*, vol. 36, no. 8, pp. 8607–8611, Aug. 2021.

[25] H. Xu, Z. Huang, Y. Yang, Z. Huang, I.-W. Iam, and C.-S. Lam, "Analysis and design of three-coil coupler for inductive power transfer system with automatic seamless CC-to-CV charging capability," *IEEE Access*, vol. 10, pp. 10139–10148, 2022.

[26] W.-J. Gu and K. Harada, "A new method to regulate resonant converters," *IEEE Trans. Power Electron.*, vol. 3, no. 4, pp. 430–439, Oct. 1988.

[27] M. Yaqoob, K. Loo, and Y. M. Lai, "Fully soft-switched dual-active-bridge series-resonant converter with switched-impedance-based power control," *IEEE Trans. Power Electron.*, vol. 33, no. 11, pp. 9267–9281, Nov. 2018.

[28] Z. Huang, C. Lam, P. Mak, R. P. D. S. Martins, S. Wong, and C. K. Tse, "A single-stage inductive-power-transfer converter for constant-power and maximum-efficiency battery charging," *IEEE Trans. Power Electron.*, vol. 35, no. 9, pp. 8973–8984, Sep. 2020.

Zhicong Huang (Member, IEEE) received the B.Eng. degree in electrical engineering and automation and the M.Eng. degree in mechanical and electronic engineering from the Huazhong University of Science and Technology, Wuhan, China, in 2010 and 2013, respectively, and the Ph.D. degree in power electronics from The Hong Kong Polytechnic University, Hong Kong, in 2018.

He is currently an Associate Professor with the Shien-Ming Wu School of Intelligent Engineering, South China University of Technology, Guangzhou, China. His current research interests include power electronics techniques in electric vehicles and power systems.

Dr. Huang received the Outstanding Reviewer Award from the IEEE Transactions on Power Electronics in 2021.

Tian Qin was born in Wuhan, China, in 1998. She received the B.Eng. degree in electrical engineering and automation from the Hubei University of Technology, Wuhan, China, in 2021. She is currently pursuing the M.Eng. degree in intelligent engineering with the Shien-Ming Wu School of Intelligent Engineering, South China University of Technology, Guangzhou, China.

Her current research interests include wireless power transfer.

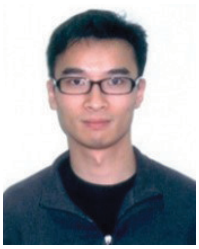

Herbert Ho-Ching Iu (Senior Member, IEEE) received the B.Eng. degree (Hons.) in electrical and electronic engineering from The University of Hong Kong, Hong Kong, in 1997, and the Ph.D. degree from The Hong Kong Polytechnic University, Hong Kong, in 2000.

In 2002, he joined the School of Electrical, Electronic and Computer Engineering, The University of Western Australia (UWA), Crawley, WA, USA, as a Lecturer, where he is currently a Professor. He has published over 150 papers in his research areas. His research interests include power electronics, renewable energy, nonlinear dynamics, current sensing techniques, and memristive systems.

Dr. Iu has won two IET Premium Awards in 2012 and 2014. In 2014, he also won the UWA Vice-Chancellor's Mid-Career Research Award. He received the 2023 IEEE TRANSACTIONS ON CIRCUITS AND SYSTEMS Guillemin-Cauer Best Paper Award, the 2021 IEEE JOURNAL OF EMERGING AND SELECTED TOPICS IN POWER ELECTRONICS Prize Paper Award, the 2019 IEEE TRANSACTIONS ON VERY LARGE SCALE INTEGRATION SYSTEMS Prize Paper Award, and the Best Paper Award of 2019 IEEE International Conference on Artificial Intelligence Circuits and Systems. He was appointed as an IEEE CASS Distinguished Lecturer for 2023–2024. He is a Coeditor of *Control of Chaos in Nonlinear Circuits and Systems* (World Scientific, Singapore, 2009) and a Coauthor of *Development of Memristor Based Circuits* (World Scientific, Singapore, 2013). He serves as the Editor-in-Chief for the IEEE JOURNAL ON SELECTED AND EMERGING TOPICS IN CIRCUITS AND SYSTEMS and an Associate Editor for the IEEE TRANSACTIONS ON CIRCUITS AND SYSTEMS II, the IEEE TRANSACTIONS ON POWER ELECTRONICS, the IEEE JOURNAL OF EMERGING AND SELECTED TOPICS ON POWER ELECTRONICS, and the IEEE TRANSACTIONS ON SMART GRID.